The SOPHIE search for northern extrasolar planets

M. J Hobson, X. Delfosse, N. Astudillo-Defru, I. Boisse, R. F. Diaz, F. Bouchy, X. Bonfils, T. Forveille, L. Arnold, S. Borgniet, et al.

A&A 625, A18 (2019)
https://doi.org/10.1051/0004-6361/201834890

Astronomy & Astrophysics

The SOPHIE search for northern extrasolar planets

XV. A warm Neptune around the M dwarf Gl 378★

M. J. Hobson[1], X. Delfosse[2], N. Astudillo-Defru[3], I. Boisse[1], R. F. Díaz[4,5], F. Bouchy[6], X. Bonfils[2], T. Forveille[2], L. Arnold[7], S. Borgniet[2], V. Bourrier[6], B. Brugger[1], N. Cabrera Salazar[2], B. Courcol[1], S. Dalal[8], M. Deleuil[1], O. Demangeon[9], X. Dumusque[6], N. Hara[6,11], G. Hébrard[8,7], F. Kiefer[8], T. Lopez[1], L. Mignon[2], G. Montagnier[8,7], O. Mousis[1], C. Moutou[1,12], F. Pepe[6], J. Rey[6], A. Santerne[1], N. C. Santos[9,10], M. Stalport[6], D. Ségransan[6], S. Udry[6], and P. A. Wilson[13,14,8]

[1] CNRS, CNES, LAM, Aix-Marseille Université, Marseille, France
e-mail: melissa.hobson@lam.fr
[2] CNRS, IPAG, Université Grenoble Alpes, 38000 Grenoble, France
[3] Departamento de Astronomía, Universidad de Concepción, Casilla 160-C, Concepción, Chile
[4] Facultad de Ciencias Exactas y Naturales, Universidad de Buenos Aires, Buenos Aires, Argentina
[5] Instituto de Astronomía y Física del Espacio (IAFE), CONICET – Universidad de Buenos Aires, Buenos Aires, Argentina
[6] Observatoire Astronomique de l'Université de Genève, 51 Chemin des Maillettes, 1290 Versoix, Switzerland
[7] Observatoire de Haute-Provence, CNRS, Aix-Marseille Université, Institut Pythéas UMS 3470, 04870 Saint-Michel-l'Observatoire, France
[8] Institut d'Astrophysique de Paris, UMR7095 CNRS, Université Pierre & Marie Curie, 98bis boulevard Arago, 75014 Paris, France
[9] Instituto de Astrofísica e Ciências do Espaço, Universidade do Porto, CAUP, Rua das Estrelas, 4150-762 Porto, Portugal
[10] Departamento de Física e Astronomia, Faculdade de Ciências, Universidade do Porto, Rua do Campo Alegre, 4169-007 Porto, Portugal
[11] ASD/IMCCE, CNRS-UMR8028, Observatoire de Paris, PSL, UPMC, 77 Avenue Denfert-Rochereau, 75014 Paris, France
[12] Canada-France-Hawaii Telescope Corporation, 65-1238 Mamalahoa Hwy, Kamuela, HI 96743, USA
[13] Department of Physics, University of Warwick, Coventry CV4 7AL, UK
[14] Centre for Exoplanets and Habitability, University of Warwick, Coventry CV4 7AL, UK

Received 15 December 2018 / Accepted 12 February 2019

ABSTRACT

We present the detection of a warm Neptune orbiting the M dwarf Gl 378, using radial velocity measurements obtained with the SOPHIE spectrograph at the Observatoire de Haute-Provence. The star was observed in the context of the SOPHIE exoplanet consortium's sub-programme dedicated to finding planets around M dwarfs. Gl 378 is an M1 star, of solar metallicity, at a distance of 14.96 pc. The single planet detected, Gl 378 b, has a minimum mass of 13.02 $M_{\rm Earth}$ and an orbital period of 3.82 days, which place it at the lower boundary of the hot Neptune desert. As one of only a few such planets around M dwarfs, Gl 378 b provides important clues to the evolutionary history of these close-in planets. In particular, the eccentricity of 0.1 may point to a high-eccentricity migration. The planet may also have lost part of its envelope due to irradiation.

Key words. techniques: radial velocities – planetary systems – stars: late-type – stars: individual: G1 378

1. Introduction

The mass-period diagram is an important diagnostic of the formation and evolution of planetary systems. There is a known dearth of Neptune-size exoplanets at short orbital periods compared to both Jupiter-size and Earth-size planets, which is generally referred to as the Neptune or sub-Jovian desert (Lecavelier Des Etangs 2007; Davis & Wheatley 2009; Szabó & Kiss 2011; Beaugé & Nesvorný 2013; Helled et al. 2016; Mazeh et al. 2016). It is unlikely to be an observational bias, but is more probably due to photoevaporation and/or high-eccentricity migration (Owen & Lai 2018; Ionov et al. 2018).

Statistics on M-dwarf planets remain less certain than those on planets around Sun-type stars, due to the comparatively small number of detections, though these detections are expected to increase thanks to several current or upcoming projects such as SPIRou (Artigau et al. 2014), CARMENES (e.g. Quirrenbach et al. 2014, 2016), HADES (e.g. Affer et al. 2016), and NIRPS (Bouchy et al. 2017) in radial velocity; or TESS (NASA mission, launched in April 2018, Ricker 2016), TRAPPIST (e.g. Gillon et al. 2017), SPECULOOS (Delrez et al. 2018), and ExTrA (Bonfils et al. 2015) in transits. Nevertheless, it is clear that while hot Jupiters are rare around M dwarfs, short-period Earths and superEarths are numerous; however, hot Neptunes remain unusual, making up only about 3% of the sample of known exoplanets around M dwarfs (e.g. Bonfils et al. 2013; Dressing & Charbonneau 2015; Hirano et al. 2018).

★ Based on observations collected with the SOPHIE spectrograph on the 1.93 m telescope at the Observatoire de Haute-Provence (CNRS), France, by the SOPHIE Consortium.

The SOPHIE exoplanet consortium has led several ongoing exoplanet-hunting programmes on the SOPHIE spectrograph at the Observatoire de Haute Provence since 2006 (Bouchy et al. 2009). Sub-programme 3, also known as SP3, is dedicated to the hunt for exoplanets around M-dwarf stars. Via a systematic survey of a volume-limited sample of M dwarfs within 12 parsecs of the Sun, it seeks to detect superEarths and Neptunes, constrain the statistics of planets around M dwarfs, and find potentially transiting companions. With a general radial velocity precision of 1–2 m s^{-1} on solar-type stars, SOPHIE has proved to be a successful planet hunter. For the SP3 in particular, we recently published the first two exoplanets from this sub-programme: the detection of Gl 96 b and the independent confirmation of Gl 617A b (Hobson et al. 2018).

In this work, we report the detection of a warm Neptune on the lower boundary of the hot Neptune desert, orbiting the M dwarf Gl 378, which was observed as part of this survey. We describe the data and its analysis in Sects. 2 and 3, respectively. The results are presented in Sect. 4 and discussed in Sect. 5. Finally, we conclude in Sect. 6.

2. Observations

Observations for Gl 378 were gathered between 2015 and 2018 with the SOPHIE+ spectrograph (Perruchot et al. 2011; Bouchy et al. 2013). A total of 62 spectra were obtained. All the observations were performed with simultaneous sky measurement in order to check for potential moonlight contamination. Additionally, a ThAr or FP calibration spectrum was obtained immediately prior to each observation in order to measure the instrumental drift (average value: 1 m s^{-1}). For the observations where the velocity difference between the moon and the star was less than 20 km s^{-1}, a merit function was applied, computed from the velocity difference and the S/N and CCF contrast in fibre B, in order to identify possible contamination. In this way, 18 observations were found to be contaminated by the moon and were discarded, leaving a total of 44 spectra. We note that retaining these observations does not change the final planetary parameters within the uncertainties, but it does increase the noise. With an exposure time of 1800 s, the spectra have a median S/N of 83 (at 650 nm), resulting in a photon noise of ≈3 m s^{-1}. For this star the photon noise is a little higher than that of instrument systematics (1–2 m s^{-1}).

3. Data analysis

The data were reduced using the SOPHIE Data Reduction Software (DRS, Bouchy et al. 2009), which computes the radial velocity (RV) by cross-correlation functions (CCF). For M dwarfs this approach does not use all the Doppler content, so we extracted RVs through a template-matching algorithm. We shifted all the spectra to a common reference frame using the DRS RVs, and co-added them to build a high S/N stellar template. This template was Doppler shifted over a series of guess RVs, producing a Chi-square profile whose minimum corresponds to the maximum likelihood RV (Astudillo-Defru et al. 2015, 2017b).

SOPHIE shows long-term variations in the zero-point, an effect first described in Courcol et al. (2015). We constructed an up-to-date correction from the SP3 stars, plus the four solar-type "super-constant" stars of the SOPHIE high-precision programmes as defined by Courcol et al. (2015), in the same way as in Hobson et al. (2018). Our updated constant correction uses ten stars: the four super-constants HD185144, HD 221354, HD 89269A, and HD 9407; the three SP3 constants Gl 411, Gl 514, and Gl 686; and the additional SP3 stars Gl 521, Gl 15A, and Gl 694, selected because they have a corrected rms after the first iteration lower than 3 m s^{-1} (as defined by Courcol et al. 2015). Figure 1 shows the correction and the data used to derive it[1].

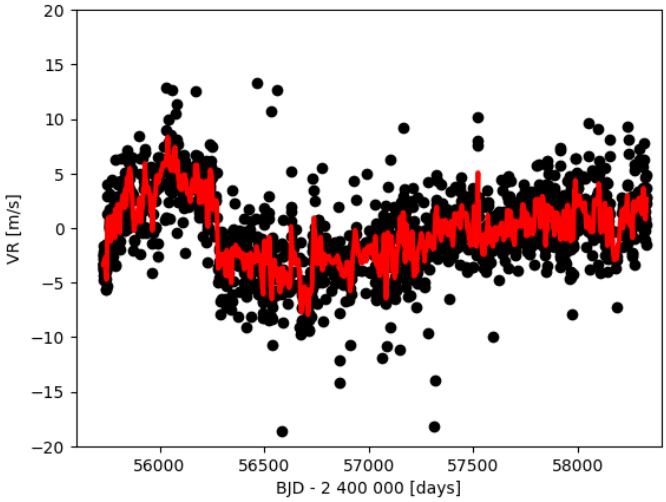

Fig. 1. Correction for the long-term variations in the zero-point (red line) and the data points used to construct it (black dots). The points correspond to the ten stars detailed in Sect. 3. The correction spans 7 yr, with a dispersion of 2.87 m s^{-1} and a peak-to-peak variation of 16.3 m s^{-1}.

The final radial velocities, which have a mean error bar of 3 m s^{-1} (including photon noise and instrumental error, following Astudillo-Defru et al. 2015), are reported in Appendix A, and were analysed with the Data and Analysis Center for Exoplanets (DACE) web platform[2]. We employed the Keplerian fitting tools (which follow Delisle et al. 2016) and the Markov chain Monte Carlo (MCMC) analysis facilities (described in Díaz et al. 2014, 2016).

3.1. Activity indicators

The main spectral activity indicators are the Hα index, the $\log(R'_{\rm HK})$ index, and the CCF bisector. We followed Boisse et al. (2009) to compute the Hα index; Astudillo-Defru et al. (2017a) to determine the $\log(R'_{\rm HK})$ index from the Ca II H and K lines measured in the spectrum; and obtained the CCF bisector from the SOPHIE DRS. Since the Na I D lines have been shown to be good activity indicators for M dwarfs (Díaz et al. 2007; Gomes da Silva et al. 2011), we also calculated the Na index as defined by Gomes da Silva et al. (2011) from our SOPHIE spectra. The values obtained are given in Appendix A.

3.2. Stellar parameters

The stellar parameters are listed in Table 1. Gl 378 was characterised in Gaidos et al. (2014), where we obtained spectral type, magnitudes and colour indices (except for the K magnitude, which was taken from Cutri et al. 2003), effective temperature, and luminosity. The coordinates, parallax, and distance were taken from the *Gaia* DR2 (Gaia Collaboration 2016, 2018). We

[1] This constant correction for SOPHIE RVs (applicable to M-dwarf stars) is available upon request.
[2] Available at https://dace.unige.ch

Table 1. Stellar parameters.

Parameter	Gl 378
Spectral type	M1 [(a)]
V	10.19 [(a)]
B–V	1.26 [(a)]
V–K	2.03 [(b)]
Mass ($M_\odot$)	0.56 ± 0.01 [(c)]
Radius ($R_\odot$)	0.56 ± 0.02 [(d)]
α (h m s)	10 02 21.7516441689 [(e)]
δ (d m s)	+48 05 19.687165248 [(e)]
Π (mas)	66.8407 ± 0.0322 [(e)]
Distance (pc)	14.9609 ± 0.0072 [(e)]
$\log(R'_{\rm HK})$	-4.98 ± 0.06 [(f)]
$T_{\rm eff}$ (K)	3879 ± 67 [(a)]
$L_\star$ ($L_\odot$)	0.06 ± 0.01 [(a)]
Fe/H (dex)	0.06 ± 0.09 [(g)]

References. [(a)]Gaidos et al. (2014). [(b)]V: Gaidos et al. (2014), K: Cutri et al. (2003). [(c)]This work, following Mann et al. (2019). [(d)]This work, following Mann et al. (2015). [(e)]Gaia Collaboration (2018). [(f)]This work, following Astudillo-Defru et al. (2017a). [(g)]This work, following Neves et al. (2014).

obtained the mean and standard deviation of $\log(R'_{\rm HK})$ from the SOPHIE spectra, and used the $\log(R'_{\rm HK}) - \log(P_{\rm rot})$ relation from Astudillo-Defru et al. (2017a) to estimate a rotation period of 40.5 ± 4 days, with error bars calculated by propagation. We employed the MCAL code of Neves et al. (2014) to estimate the metallicity from our SOPHIE spectra. Finally, we used the distance measurement from Gaia Collaboration (2018) to estimate a more precise radius (following Mann et al. 2015, with errors calculated by propagation) and stellar mass (using the MCMC routine provided by Mann et al. 2019, based on masses from Delfosse et al. 2000) than were available in the literature.

4. Results

The time series of the radial velocities is shown in Fig. 2, and its periodogram in Fig. 3. The periodogram shows a clear peak at 3.82 d, which by bootstrap resampling we place below a 0.01% false alarm probability (FAP). The other notable peaks, at 0.79 d and 1.35d, are 1-day aliases of the 3.82 d period; they are systematically weaker than the 3.82 d peak, and attempted Keplerian fits have higher $\sigma_{\rm (O-C)}$. We also computed the l1-periodogram as in Hara et al. (2017), which is shown in Fig. 4, and confirms the 3.82 d signal as the most significant.

The periodograms of the four activity indicators described in Sect. 3.1 are shown in Fig. 5. None of them shows any peaks below 10% FAP, or any peak whatsoever at the 3.82 d period found in the RVs. Likewise, there is no anti-correlation in evidence between the RVs and the CCF bisector. Additionally, for an M dwarf, a rotation period of 3.82 d would lead to an extremely high activity level, with saturated chromospheric emission of Hα (Delfosse et al. 1998) and Ca (Astudillo-Defru et al. 2017a), which is clearly not the case for Gl 378. Finally, Houdebine (2010) found Gl 378 to be a slow rotator, with $v \sin i = 2.25$ km s^{-1}. Therefore, we conclude that the 3.82 d peak cannot be of stellar origin, and that Gl 378 shows no evidence of clear stellar activity (at the estimated rotation period of $P_{\rm Rot} = 40.5 \pm 4$ d, indicated by the shaded grey regions in Fig. 5, or any other period) in the SOPHIE spectra.

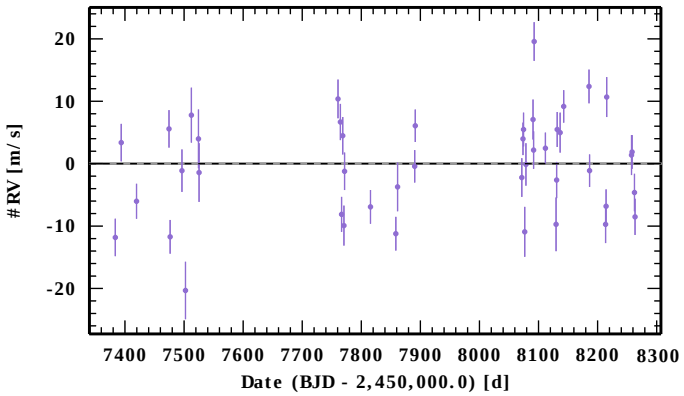

Fig. 2. SOPHIE RVs for Gl 378, obtained using template-matching, and corrected for the nightly drift and the long-term variations of the zero-point.

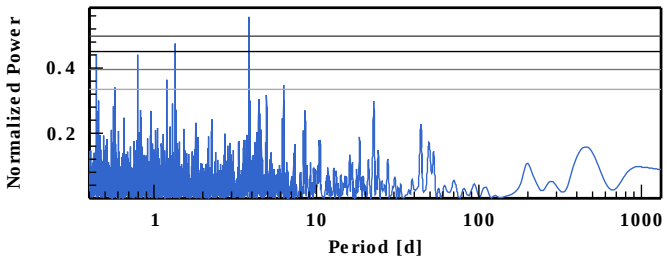

Fig. 3. Periodogram of the SOPHIE RVs for Gl 378, obtained using template-matching, and corrected for the nightly drift and the long-term variations of the zero-point. The horizontal lines indicate the 50, 10, 1, and 0.1% FAP levels (from bottom to top).

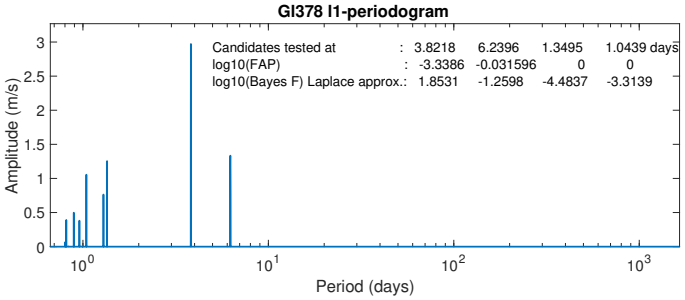

Fig. 4. l1-periodogram following Hara et al. (2017). The FAP is computed according to the Baluev (2008) formula, and the Bayes factor is computed via a Laplace approximation with the same methodology as in Nelson et al. (2018, Appendix A.4).

We employed the DACE platform to fit a Keplerian signal to the 3.82 d period. The highest peak in the periodogram of the residuals has a FAP of 17%, and is therefore not significant (Fig. 6). In order to sample the joint posterior distribution of the model parameters, we carried out an MCMC analysis. We used a model with a single Keplerian and an additive stellar jitter. The resulting parameters are summarised in Table 2, with the full outputs available in Appendix B. The phase-folded data and fitted Keplerian are shown in Fig. 7.

5. Discussion

With a minimum mass of 13.63 $M_{\rm Earth}$ and an orbital period of 3.82 d, Gl 378 b is a warm Neptune-like exoplanet. Depending on the heat redistribution factor and albedo assumed, we obtain

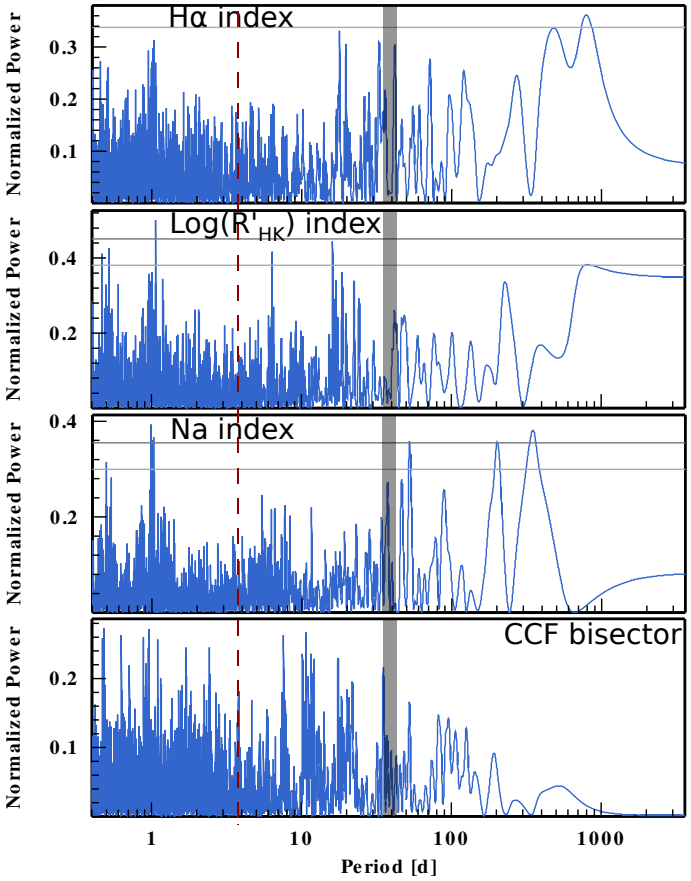

Fig. 5. Periodogram of the activity indices for Gl 378. *From top to bottom panels*: Hα index, log($R'_{\rm HK}$) index, Na index, and CCF bisector. The horizontal lines indicate the 50 and 10% FAP levels. The red vertical dashed line marks the orbital period of Gl 378 b. The shaded grey region indicates the probable rotation period, as estimated from the log($R'_{\rm HK}$).

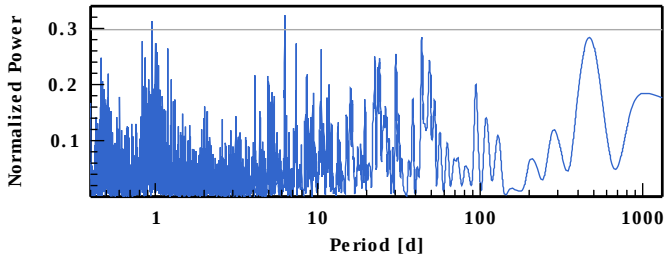

Fig. 6. Periodogram of the residuals of the SOPHIE RVs for Gl 378 following the fit of a planet at 3.82 d. The horizontal line indicates the 50% FAP level.

equilibrium temperatures in the range of $T_{\rm eq} \approx 630$ K (for a heat redistribution factor of 1 and an albedo of 0.3, close to that of Neptune) to $T_{\rm eq} \approx 830$ K (for a redistribution factor of 2 and an albedo of 0, as a lower limit). Its orbital parameters place it on the lower boundary of the Neptune desert as defined by Mazeh et al. (2016), as shown in Fig. 8, although they note that the lower boundary is somewhat blurry, and other authors (e.g. Owen & Lai 2018) have placed the external limit in period at $P \approx 3$ d rather than $P \approx 5$ d. This location on the lower boundary rather than within the desert, and its range of probable equilibrium temperature well below the methane condensation temperature of 1200 K, lead us to classify it as a warm rather than a hot Neptune.

Table 2. Best-fit solution for the planetary system orbiting Gl 378.

Param.	Units	Gl 378 b
P	(d)	$3.822^{+0.001}_{-0.001}$
K	(m s^{-1})	$7.96^{+1.24}_{-1.23}$
e		$0.109^{+0.131}_{-0.077}$
ω	(deg)	$210.6^{+79.8}_{-116.9}$
T_P	(d)	$2455500.02^{+1.27}_{-1.3}$
T_C	(d)	$2455502.564^{+0.72}_{-1.05}$
a	(AU)	$0.039435^{+0.00023}_{-0.00023}$
$M \sin i$	($M_{\rm Earth}$)	$13.02^{+2.03}_{-2.01}$
$\gamma_{\rm SOPHIE}$	(m s^{-1})	$-9697.333^{+0.85}_{-0.83}$
$\sigma_{\rm JIT}$	(m s^{-1})	$4.610^{+0.83}_{-0.74}$
$\sigma_{\rm (O-C)}$	(m s^{-1})	4.86
log (Likelihood)		$-138.07^{+1.41}_{-2.09}$

Notes. For each parameter the median of the posterior is given, with error bars computed from the MCMC analysis using a 68.3% confidence interval. $\sigma_{\rm O-C}$ corresponds to the weighted standard deviation of the residuals around the best solutions. All the parameters probed by the MCMC can be found in Table B.1.

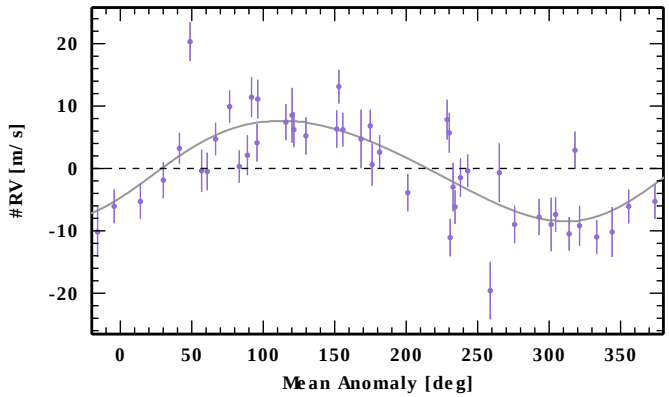

Fig. 7. SOPHIE RVs for Gl 378, phase-folded to the one-planet model with $P = 3.82$ d. The curve indicates the fitted model.

The lower boundary is believed to have its origin in photoevaporation (Owen & Lai 2018). Therefore, Gl 378 b may have lost at least part of its gaseous envelope due to the X-ray and EUV irradiation from its host star. We note that the young active phase is long for M dwarfs compared to Sun-type stars, giving more time for evaporation to work.

If we assume that the mass of Gl 378 b is close to its $M \sin i$, it is likely similar to GJ 436 b (Ehrenreich et al. 2015; Lavie et al. 2017) and GJ 3470 b (Bourrier et al. 2018a). These planets are warm Neptunes, in the same region of the mass-period diagram as Gl 378 b (Fig. 8), and orbit M-dwarf stars. Both are surrounded by giant hydrogen exospheres; GJ 436b possibly became a warm Neptune recently due to a late high-eccentricity migration and is thus currently not losing much mass (Bourrier et al. 2015, 2016, 2018b), while GJ 3470b is much more irradiated by its younger and earlier-type star and could have lost up to 35% of its mass already (Bourrier et al. 2018a). This suggests that the warm Neptune population at the border of the desert is particularly sensitive to atmospheric escape, and

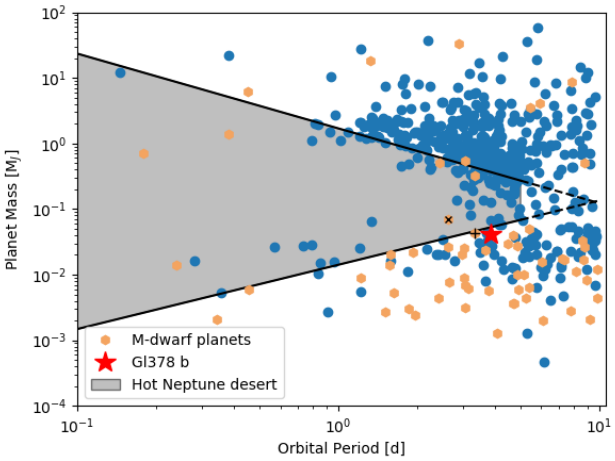

Fig. 8. Hot Neptune desert. Gl 378 b is indicated by the red star. All planets with known masses and periods <10 d are shown (taken from exoplanets.eu on 18 Oct. 2018). Planets orbiting M dwarfs are highlighted (orange hexagons); GJ 436 b and GJ 3470 are indicated by cross (×) and plus signs (+), respectively. The location of the hot Neptune desert is indicated (grey region), using the boundaries of Mazeh et al. (2016; black lines). The boundaries are dotted beyond 5 d, which reflects the Mazeh et al. (2016) warning that beyond this orbital period the existence of the desert is uncertain.

supports this mechanism as the reason why hot Neptunes are missing. The three planets also have similar non-zero eccentricities (Deming et al. 2007; Kosiarek et al. 2019), which may point to high-eccentricity rather than disk-driven migrations. Therefore, objects like Gl 378 b are crucial to understanding the evolution of close-in planets, providing we can characterise them.

A fuller characterisation of the planet would require knowledge of its density, and therefore of its radius. The transit probability of a planet detected by radial velocity can be approximated by $P(\text{transit}) \approx R_\star/a$, with $R_\star$ the stellar radius and a the semi-major axis of the planetary orbit (Borucki & Summers 1984). For Gl 378 b, we obtain a transit probability of $P(\text{transit}) = 6.5 \pm 0.5\%$. As Gl 378 b is most likely a Neptune-mass exoplanet, the analysis of Stevens & Gaudi (2013) suggests this transit probability is likely underestimated: they derive the posterior transit probability from the prior distributions of planetary masses and inclinations, finding that physically motivated distributions from planet formation models yield increased posterior transit probabilities for Neptune-mass planets. The transit depth is given by $\Delta F = (R_\text{p}/\text{R}_\star)^2$. Using the mass-radius relation of Chen & Kipping (2017), we estimate the radius of Gl 378 b as $R_\text{p} \approx 4.67\,R_\oplus$; when combined with the stellar radius, this value gives a transit depth of $\Delta F \approx 0.58\%$. This could be observed by ground-based surveys, and should be easily detectable by space-based missions such as TESS (Barclay et al. 2018) or CHEOPS (Rando et al. 2018).

The metallicity estimated for the host star, Gl 378, from our SOPHIE spectra is $[\text{Fe/H}] = 0.06 \pm 0.09$. This solar metallicity is in line with the tendency for M dwarfs hosting planets to be comparatively more metal rich (e.g. Courcol et al. 2016, Hirano et al. 2018, who find $[\text{Fe/H}] \gtrsim 0$ for planet hosts) with respect to the sub-solar average metallicity of nearby M dwarfs (e.g. Schlaufman & Laughlin 2010, who report $[\text{Fe/H}] = -0.17 \pm 0.07$, and Passegger et al. 2018, who find mainly subsolar values for the CARMENES target sample) and also with findings that hot Neptunes are more common with increasing metallicity (Petigura et al. 2018, although it is a study on the Kepler survey where the planets are thus categorised by radius rather than mass).

The activity indicators analysed show no evidence for quasi-periodic stellar activity signals. Likewise, the residuals of the Keplerian fit to the 3.82 d planet show no significant periodicity, although statistics on M dwarfs indicate that most of their planets are found in multi-planet systems (e.g. Bonfils et al. 2013; Dressing & Charbonneau 2015). However, the $\sigma_{\text{O–C}}$ (weighted standard deviation of the residuals around the best solution) is high compared to the mean error bar of the observations, suggesting that there are further effects in the data, i.e. additional planets, stellar activity signals, and/or systematics. As an M dwarf, Gl 378 is faint in the visible, emitting most of its radiation in the infrared; consequently, high-precision infrared spectroscopy could help to detect further planets or place limits on their existence.

6. Conclusions

We have presented the detection of a Neptune-mass planet orbiting the M dwarf Gl 378 at a period of 3.82 d. Its orbital parameters place it at the edge of the hot Neptune desert, though with a $\sin(i)$ degeneracy on the mass. Transit observations could help to break this degeneracy: if the planet transits the inclination can be measured, while a non-detection can place limits on it. Transit measurements would also provide the radius and therefore the density, permitting a characterisation of its probable composition. Finally, if the planet transits, we should be able to characterise its atmosphere in the UV/Ly-α line, given the brightness and close distance of its host star to us, and because the planet is a warm Neptune and therefore likely surrounded by a giant hydrogen exosphere. This exosphere can extend beyond the Roche lobe, resulting in an effective planet radius in UV an order of magnitude larger than the optical radius, and hence a slightly increased transit probability. Therefore, UV/Ly-α observations at the expected transit times would be interesting even if the planet does not transit in the optical.

Although we do not detect any other periodic signals in our data, it is statistically likely that more planets are present. Monitoring this star with infrared spectroscopy should help to resolve this question, and to refine the ephemeris of Gl 378b for transit searches. We hope to observe Gl 378 with SPIRou in the near future.

Acknowledgements. We warmly thank the OHP staff for their support on the observations. We thank the anonymous referee for the careful reading and valuable comments which helped to improve the manuscript. This work was supported by the Programme National de Planétologie (PNP) of CNRS/INSU, co-funded by CNE. X.De., X.B., I.B., and T.F. received funding from the French Programme National de Physique Stellaire (PNPS) and the Programme National de Planétologie (PNP) of CNRS (INSU). X.B. acknowledges funding from the European Research Council under the ERC Grant Agreement n. 337591-ExTrA. This work has been supported by a grant from Labex OSUG@2020 (Investissements d'avenir – ANR10 LABX56). This work is also supported by the French National Research Agency in the framework of the Investissements d'Avenir program (ANR-15-IDEX-02), through the funding of the "Origin of Life" project of the Univ. Grenoble-Alpes. V.B. acknowledges support from the Swiss National Science Foundation (SNSF) in the frame of the National Centre for Competence in Research PlanetS, and has received funding from the European Research Council (ERC) under the European Unions Horizon 2020 research and innovation programme (project Four Aces; grant agreement No 724427). This work was supported by FCT – Fundação para a Ciência e a Tecnologia through national funds and by FEDER through COMPETE2020 – Programa Operacional Competitividade e Internacionalização by grants UID/FIS/04434/2013 & POCI-01-0145-FEDER-007672; PTDC/FIS-AST/28953/2017 & POCI-01-0145-FEDER-028953; and PTDC/FIS-AST/32113/2017 & POCI-01-0145-FEDER-032113. N.A-D. acknowledges support from FONDECYT #3180063. N.H.

acknowledges the financial support of the National Centre for Competence in Research PlanetS of the Swiss National Science Foundation (SNSF). X.Du. is grateful to the Branco Weiss Fellowship–Society in Science for continuous support. This publication makes use of the Data & Analysis Center for Exoplanets (DACE), which is a facility based at the University of Geneva (CH) dedicated to extrasolar planets data visualisation, exchange, and analysis. DACE is a platform of the Swiss National Centre of Competence in Research (NCCR) PlanetS, federating the Swiss expertise in Exoplanet research. The DACE platform is available at https://dace.unige.ch.

References

Affer, L., Micela, G., Damasso, M., et al. 2016, A&A, 593, A117
Artigau, É., Kouach, D., Donati, J.-F., et al. 2014, in Ground-based and Airborne Instrumentation for Astronomy V, Proc. SPIE, 9147, 914715
Astudillo-Defru, N., Bonfils, X., Delfosse, X., et al. 2015, A&A, 575, A119
Astudillo-Defru, N., Delfosse, X., Bonfils, X., et al. 2017a, A&A, 600, A13
Astudillo-Defru, N., Díaz, R. F., Bonfils, X., et al. 2017b, A&A, 605, L11
Baluev, R. V. 2008, MNRAS, 385, 1279
Barclay, T., Pepper, J., & Quintana, E. V. 2018, ApJS, 239, 2
Beaugé, C., & Nesvorný, D. 2013, ApJ, 763, 12
Boisse, I., Moutou, C., Vidal-Madjar, A., et al. 2009, A&A, 495, 959
Bonfils, X., Delfosse, X., Udry, S., et al. 2013, A&A, 549, A109
Bonfils, X., Almenara, J. M., Jocou, L., et al. 2015, in Techniques and Instrumentation for Detection of Exoplanets VII, Proc. SPIE, 9605, 96051L
Borucki, W. J., & Summers, A. L. 1984, Icarus, 58, 121
Bouchy, F., Hébrard, G., Udry, S., et al. 2009, A&A, 505, 853
Bouchy, F., Díaz, R. F., Hébrard, G., et al. 2013, A&A, 549, A49
Bouchy, F., Doyon, R., Artigau, É., et al. 2017, The Messenger, 169, 21
Bourrier, V., Ehrenreich, D., & Lecavelier des Etangs, A. 2015, A&A, 582, A65
Bourrier, V., Lecavelier des Etangs, A., Ehrenreich, D., Tanaka, Y. A., & Vidotto, A. A. 2016, A&A, 591, A121
Bourrier, V., Lecavelier des Etangs, A., Ehrenreich, D., et al. 2018a, A&A, 620, A147
Bourrier, V., Lovis, C., Beust, H., et al. 2018b, Nature, 553, 477
Chen, J., & Kipping, D. 2017, ApJ, 834, 17
Courcol, B., Bouchy, F., Pepe, F., et al. 2015, A&A, 581, A38
Courcol, B., Bouchy, F., & Deleuil, M. 2016, MNRAS, 461, 1841
Cutri, R. M., Skrutskie, M. F., van Dyk, S., et al. 2003, VizieR Online Data Catalog: II/246
Davis, T. A., & Wheatley, P. J. 2009, MNRAS, 396, 1012
Delfosse, X., Forveille, T., Perrier, C., & Mayor, M. 1998, A&A, 331, 581
Delfosse, X., Forveille, T., Ségransan, D., et al. 2000, A&A, 364, 217
Delisle, J.-B., Ségransan, D., Buchschacher, N., & Alesina, F. 2016, A&A, 590, A134
Delrez, L., Gillon, M., Queloz, D., et al. 2018, SPIE Conf. Ser., 10700, 107001I
Deming, D., Harrington, J., Laughlin, G., et al. 2007, ApJ, 667, L199
Díaz, R. F., Cincunegui, C., & Mauas, P. J. D. 2007, MNRAS, 378, 1007
Díaz, R. F., Almenara, J. M., Santerne, A., et al. 2014, MNRAS, 441, 983
Díaz, R. F., Ségransan, D., Udry, S., et al. 2016, A&A, 585, A134
Dressing, C. D., & Charbonneau, D. 2015, ApJ, 807, 45
Ehrenreich, D., Bourrier, V., Wheatley, P. J., et al. 2015, Nature, 522, 459
Gaia Collaboration (Prusti, T., et al.) 2016, A&A, 595, A1
Gaia Collaboration (Brown, A. G. A., et al.) 2018, A&A, 616, A1
Gaidos, E., Mann, A. W., Lépine, S., et al. 2014, MNRAS, 443, 2561
Gillon, M., Triaud, A. H. M. J., Demory, B.-O., et al. 2017, Nature, 542, 456
Gomes da Silva, J., Santos, N. C., Bonfils, X., et al. 2011, A&A, 534, A30
Hara, N. C., Boué, G., Laskar, J., & Correia, A. C. M. 2017, MNRAS, 464, 1220
Helled, R., Lozovsky, M., & Zucker, S. 2016, MNRAS, 455, L96
Hirano, T., Dai, F., Gandolfi, D., et al. 2018, AJ, 155, 127
Hobson, M. J., Díaz, R. F., Delfosse, X., et al. 2018, A&A, 618, A103
Houdebine, E. R. 2010, MNRAS, 407, 1657
Ionov, D. E., Pavlyuchenkov, Y. N., & Shematovich, V. I. 2018, MNRAS, 476, 5639
Kosiarek, M. R., Crossfield, I. J. M., Hardegree-Ullman, K. K., et al. 2019, AJ, 157, 97
Lavie, B., Ehrenreich, D., Bourrier, V., et al. 2017, A&A, 605, L7
Lecavelier Des Etangs, A. 2007, A&A, 461, 1185
Mann, A. W., Feiden, G. A., Gaidos, E., Boyajian, T., & von Braun, K. 2015, ApJ, 804, 64
Mann, A. W., Dupuy, T., Kraus, A. L., et al. 2019, ApJ, 871, 63
Mazeh, T., Holczer, T., & Faigler, S. 2016, A&A, 589, A75
Nelson, B. E., Ford, E. B., Buchner, J., et al. 2018, ArXiv e-prints [arXiv:1806.04683]
Neves, V., Bonfils, X., Santos, N. C., et al. 2014, A&A, 568, A121
Owen, J. E., & Lai, D. 2018, MNRAS, 479, 5012
Passegger, V. M., Reiners, A., Jeffers, S. V., et al. 2018, A&A, 615, A6
Perruchot, S., Bouchy, F., Chazelas, B., et al. 2011, in Techniques and Instrumentation for Detection of Exoplanets V, Proc. SPIE, 8151, 815115
Petigura, E. A., Marcy, G. W., Winn, J. N., et al. 2018, AJ, 155, 89
Quirrenbach, A., Amado, P. J., Caballero, J. A., et al. 2014, in Ground-based and Airborne Instrumentation for Astronomy V, Proc SPIE, 9147, 91471F
Quirrenbach, A., Amado, P. J., Caballero, J. A., et al. 2016, in Ground-based and Airborne Instrumentation for Astronomy VI, Proc. SPIE, 9908, 990812
Rando, N., Asquier, J., Corral Van Damme, C., et al. 2018, SPIE Conf. Ser., 10698, 106980K
Ricker, G. R. 2016, AGU Fall Meeting Abstracts, P13C-01
Schlaufman, K. C., & Laughlin, G. 2010, A&A, 519, A105
Stevens, D. J., & Gaudi, B. S. 2013, PASP, 125, 933
Szabó, G. M., & Kiss, L. L. 2011, ApJ, 727, L44

Appendix A: Radial velocities

In this appendix, we present the radial velocities obtained for Gl 378 from SOPHIE+ using template-matching, corrected for the nightly drift and the long-term variations of the zero-point.

Table A.1. Radial velocities for Gl 378.

BJD (−2400000 d)	RV (km s^{-1})	σ_{RV} (km s^{-1})	Bisector (m s^{-1})	Hα index	$\sigma_{H\alpha}$	$\log(R'_{HK})$	$\sigma_{\log(R'_{HK})}$	Na index	σ_{Na}
57 383.6037	−9.7084	0.003	15.167	0.2353	0.0012	−4.9599	0.0001	0.2107	0.0103
57 393.6361	−9.6932	0.003	11.333	0.2242	0.0012	−4.9868	0.0001	0.2116	0.0101
57 419.5259	−9.7026	0.0028	−2	0.2255	0.0011	−4.9107	0.0001	0.2085	0.0094
57 474.4968	−9.691	0.003	20.667	0.2236	0.0012	−5.0253	0.0001	0.2079	0.0100
57 476.428	−9.7083	0.0027	21.333	0.2248	0.0010	−5.002	0.0001	0.2045	0.0089
57 496.4268	−9.6977	0.0034	16.333	0.2343	0.0015	−4.9589	0.0001	0.2163	0.0110
57 502.3933	−9.7169	0.0046	−8.667	0.2386	0.0021	−4.9313	0.0001	0.2212	0.0145
57 512.3882	−9.6888	0.0044	13	0.2267	0.0019	−4.9842	0.0001	0.2115	0.0139
57 524.3675	−9.6926	0.0047	−1	0.2389	0.0022	−5.0567	0.0001	0.2199	0.0156
57 525.3946	−9.698	0.0047	−1.333	0.2416	0.0022	−5.0498	0.0001	0.214	0.0150
57 760.5835	−9.6862	0.0031	15.167	0.2227	0.0013	−4.9891	0.0001	0.217	0.0104
57 764.615	−9.6899	0.0029	7.167	0.2223	0.0012	−4.9965	0.0001	0.2174	0.0101
57 766.6183	−9.7047	0.0028	5.333	0.2258	0.0011	−5.0322	0.0001	0.2127	0.0010
57 768.5861	−9.6921	0.003	8.167	0.2228	0.0012	−4.9964	0.0001	0.2254	0.0105
57 770.6187	−9.7065	0.0032	3	0.2263	0.0013	−5.0235	0.0001	0.2221	0.0111
57 771.6751	−9.6978	0.003	18	0.2226	0.0012	−5.0034	0.0001	0.2163	0.0101
57 815.5618	−9.7035	0.0027	11.833	0.222	0.0011	−5.0024	0.0001	0.2122	0.0093
57 858.4545	−9.7078	0.0027	10.333	0.232	0.0010	−4.996	0.0001	0.2051	0.0092
57 861.4145	−9.7003	0.0039	19.5	0.2341	0.0017	−5.0434	0.0001	0.2229	0.0129
57 890.4053	−9.697	0.0026	13.5	0.2314	0.0009	−4.9607	0.0001	0.1997	0.0084
57 891.3779	−9.6905	0.0026	10	0.2285	0.0009	−4.9447	0.0001	0.2038	0.0086
58 071.6969	−9.6988	0.0031	15	0.2358	0.0012	−4.9848	0.0001	0.2123	0.0104
58 073.6999	−9.6926	0.0026	9.833	0.2326	0.0010	−4.9674	0.0001	0.2074	0.0092
58 074.6453	−9.6911	0.0027	21	0.2421	0.0010	−4.9242	0.0001	0.2085	0.0094
58 076.6457	−9.7075	0.004	3.167	0.233	0.0018	−4.9704	0.0001	0.2162	0.0130
58 078.6855	−9.6967	0.0034	2	0.2365	0.0014	−4.9643	0.0001	0.2133	0.0110
58 090.7094	−9.6895	0.0032	3.333	0.2317	0.0014	−4.941	0.0001	0.2131	0.0108
58 091.6594	−9.6944	0.003	4.333	0.2339	0.0012	−4.9547	0.0001	0.2121	0.0102
58 092.6222	−9.677	0.0031	7.833	0.2373	0.0013	−4.9128	0.0001	0.2173	0.0107
58 111.6548	−9.6941	0.0025	15	0.254	0.0010	−4.8508	0.0001	0.2127	0.0091
58 129.7054	−9.7063	0.0043	0.333	0.2243	0.0019	−4.9616	0.0001	0.2457	0.0146
58 130.6467	−9.6992	0.0029	14.667	0.2311	0.0011	−4.9647	0.0001	0.2151	0.0010
58 131.6165	−9.6911	0.0028	3.333	0.2299	0.0011	−4.9829	0.0001	0.211	0.0097
58 136.5933	−9.6916	0.0032	8.833	0.2296	0.0014	−4.9599	0.0001	0.2241	0.0111
58 142.6058	−9.6874	0.0026	11.167	0.2363	0.0010	−4.9272	0.0001	0.2125	0.0094
58 185.4633	−9.6842	0.0027	4.833	0.2277	0.0010	999.99	0.0001	0.215	0.0093
58 186.4198	−9.6977	0.0026	8	0.2313	0.0010	999.99	0.0001	0.2103	0.0089
58 213.5248	−9.7063	0.003	15.833	0.2405	0.0011	999.99	0.0001	0.2094	0.0097
58 214.3723	−9.7034	0.0027	11.833	0.2334	0.0010	999.99	0.0001	0.2095	0.0092
58 215.3927	−9.6859	0.0032	14.833	0.2378	0.0013	999.99	0.0001	0.2147	0.0103
58 257.4077	−9.6952	0.0032	10.667	0.2226	0.0012	999.99	0.0001	0.2029	0.0099
58 258.3895	−9.6947	0.0027	5.5	0.2254	0.0010	999.99	0.0001	0.2029	0.0090
58 262.4213	−9.7012	0.003	11.5	0.2231	0.0011	999.99	0.0001	0.2035	0.0097
58 263.3966	−9.7051	0.0029	7.667	0.2248	0.0011	999.99	0.0001	0.2006	0.0093

Appendix B: MCMC parameters

In this appendix we present the parameters probed by the MCMC analysis that was applied to the radial velocities of Gl 378.

Table B.1. Parameters probed by the MCMC used to fit the RV measurements of Gl 378.

Parameter	Units	Max(Likelihood)	Mode	Mean	Std	Median	68.27%	95.45%	99.73%	Prior
log(Likelihood)		−135.12	−137.44	−138.41	1.85	−138.07	[−140.16 to 136.66]	[−143.08 to 135.84]	[−147.57 to 135.37]	–
						Star				
M_S	($M_\odot$)	0.5458	0.5591	0.5600	0.0100	0.5599	[0.5500–0.5699]	[0.5399–0.5801]	[0.5297–0.5900]	$\mathcal{U}$
Π_S	(mas)	66.8313	66.8364	66.8405	0.0322	66.8402	[66.8083–66.8721]	[66.7762–66.9052]	[66.7465–66.9380]	$\mathcal{U}$
						Offset				
$\gamma_{\mathrm{NAIRA(DRS-errinc3)}}$	($m\,s^{-1}$)	−9697.488	−9697.317	−9697.329	0.864	−9697.333	[−9698.165 to 9696.485]	[−9699.075 to 9695.588]	[−9700.136 to 9694.614]	$\mathcal{U}$
						Noise				
Avg. act.	($m\,s^{-1}$)	4.073	4.521	4.664	0.806	4.610	[3.874–5.441]	[3.199–6.417]	[2.658–7.737]	$\mathcal{U}(0,20)$
						Gl 378b				
P	(d)	3.82264	3.82248	3.82249	0.00135	3.82248	[3.82119–3.82381]	[3.81973–3.82522]	[3.81806–3.82698]	$\mathcal{U}$
K	($m\,s^{-1}$)	8.16	7.91	7.96	1.24	7.96	[6.73–9.20]	[5.51–10.47]	[4.19–11.95]	$\mathcal{U}$
e		0.098	0.000	0.132	0.103	0.109	[0.032–0.234]	[0.004–0.393]	[0.000–0.595]	$\mathcal{U}$
ω	(°)	218.4	244.6	197.0	90.7	210.6	[93.7–290.4]	[13.1–346.8]	[0.8–359.4]	$\mathcal{U}$
λ_0	(°)	203.8	197.3	190.8	76.3	192.3	[113.5–270.3]	[26.3–337.0]	[1.1–358.6]	$\mathcal{U}$
a_S	(AU)	0.000002853	0.000002750	0.000002756	0.000000426	0.000002755	[0.000002329–0.000003180]	[0.000001904–0.000003612]	[0.000001437–0.000004076]	–-
a	(AU)	0.039102	0.039416	0.039436	0.000235	0.039435	[0.039200–0.039668]	[0.038960–0.039906]	[0.038709–0.040128]	–
m	($M_\oplus$)	13.26	13.03	13.03	2.02	13.02	[11.01–15.05]	[8.99–17.09]	[6.73–19.17]	–
m	(M_J)	0.04172	0.04100	0.04100	0.00636	0.04098	[0.03464–0.04736]	[0.02828–0.05378]	[0.02116–0.06033]	–
m	($M_\odot$)	0.00003982	0.00003913	0.00003914	0.00000607	0.00003911	[0.00003306–0.00004521]	[0.00002699–0.00005133]	[0.00002020–0.00005759]	–
T_C	(BJD)	2455501.200	2455502.749	2455502.399	0.918	2455502.564	[2455501.511–2455503.286]	[2455500.131–2455503.723]	[2455500.011–2455503.815]	–
T_P	(BJD)	2455500.16	2455500.42	2455500.00	1.09	2455500.02	[2455498.72–2455501.29]	[2455498.18–2455501.83]	[2455498.09–2455501.91]	–

Notes. The maximum likelihood solution, median, mode, and standard-deviation of the posterior distribution for each parameter are shown, as well as the 68.27, 95.45, and 99.73% confidence intervals. Parameters with priors listed are fitting parameters, while the rest are derived. The prior for each parameter can be of the following types: $\mathcal{U}$: uniform, $\mathcal{N}$: normal, or $\mathcal{TN}$: truncated normal. Priors without given ranges are improper. The mean longitude λ_0 is given at reference epoch: 2 455 500.0 BJD.